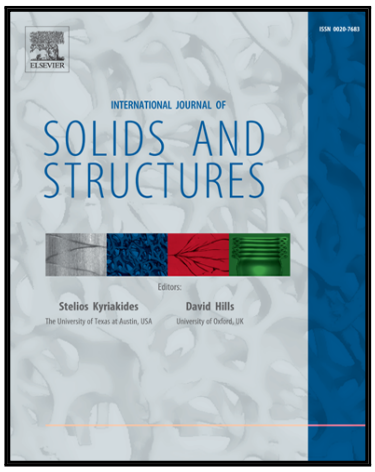

A 3D computational model of electrospun networks and its application to inform a reduced modelling approach

Sebastian Domaschke, Manuel Zündel, Edoardo Mazza, Alexander E. Ehret

PII: S0020-7683(18)30356-1
DOI: https://doi.org/10.1016/j.ijsolstr.2018.08.030
Reference: SAS 10104

To appear in: *International Journal of Solids and Structures*

Received date: 25 January 2018
Revised date: 3 July 2018
Accepted date: 31 August 2018

Please cite this article as: Sebastian Domaschke, Manuel Zündel, Edoardo Mazza, Alexander E. Ehret, A 3D computational model of electrospun networks and its application to inform a reduced modelling approach, *International Journal of Solids and Structures* (2018), doi: https://doi.org/10.1016/j.ijsolstr.2018.08.030

A 3D computational model of electrospun networks and its application to inform a reduced modelling approach

Sebastian Domaschke [☆a,b,*], Manuel Zündel[☆b], Edoardo Mazza[a,b], Alexander E. Ehret[a,b,*]

[a] *Empa, Swiss Federal Laboratories for Materials Science and Technology, 8600 Dübendorf, Switzerland*
[b] *ETH Zurich, Institute for Mechanical Systems, 8092 Zurich, Switzerland*

Abstract

In this contribution, a full 3D finite element model of electrospun networks is presented. The model explicitly accounts for the specific microstructure of these networks by generating representative volume elements through a particular fibre deposition method inspired by the process of network formation during electrospinning. The modelled fibre material and structural properties, such as different fibre shapes and distributions in diameter, can vary over a wide range, and mutual fibre contact is considered in addition to permanent cross-links. In addition to the homogenized mechanical response to macroscopic in-plane loads, the model provides access to structural information which can hardly be determined in experiments, such as fibre disposition and interconnectivity. In the present work, this asset is used to inform a recent 2.5D modelling approach (Zündel et al., 2017) and to validate inherent assumptions on network structure. The comparison between the responses of the two approaches reveals that for networks of high porosity, the reduced 2.5D model captures well the mechanical behaviour in plane stress load cases. At lower porosities though, the increasing out-of-plane orientation of fibre segments leads to effects that cannot be captured by planar approaches and necessitate a 3D approach.

Keywords:
Multiscale modelling, Fibrous material, Electrospun network, Discrete network model, Finite element analysis

1. Introduction

Electrospinning is a simple, cost-efficient and versatile technique to produce non-woven meshes with nano- to micrometer sized polymeric fibres [1, 2]. The versatility of the process permits scaffold architectures and properties within a wide range, rendering electrospun fabrics potential candidates for various technical applications, such as filters, catalyst carriers, sensors or sound absorbent materials [3], and for biomedical use, particularly as scaffolds for tissue engineering [3, 4].

Briefly, the basic set up of the electrospinning process is as follows [5]: A polymer solution or melt is pumped to a needle that is placed in fixed distance from a usually grounded collector and connected to a high voltage power supply. The difference of electric potential (~10-30 kV [6]) generates an electric field, which causes the droplet of polymer solution at the needle tip to deform into a cone shape [7, 8]. When the electrostatic repulsion forces overcome the surface tension at a critical voltage, a continuous jet is ejected and extremely elongated while the solvent evaporates and the jet solidifies. The so-formed fibres deposit on top of the previously spun material on the collector and form a highly porous network. While at fibre length scale (~µm) these electrospun networks are discrete structures with mechanics governed by the properties of fibres and their mutual interactions, they appear continuous at the macroscopic scale (~mm), characterised by the homogenised response of its microstructural constituents. Depending on the application, different requirements are posed to the two scales [cf. 9], which can be addressed by tailoring the network through the tuning of the electrospinning process parameters. The relation between fibre properties

[☆] Both authors contributed equally to this work.
[*] Corresponding authors (sebastian.domaschke@empa.ch, alexander.ehret@empa.ch).

and network microstructure on the one hand and the macroscopic mechanical behaviour on the other hand can be analysed experimentally after spinning. However, the many different results that can be obtained with the multifarious electrospinning process drastically increase the number of experiments required for systematic studies, and make the identification of networks with dedicated micro- and macroscopic properties a demanding task. In this regard, predictive multi-scale models able to account for the interdependency between the length scales provide a useful alternative, at least to narrow down the many options that exist in terms of materials and their organization.

The macroscopic mechanical behaviour of ESNs has been captured by continuum models without or very little reference to their microscopic properties [10–13]. In addition, few models were proposed that established scale transitions by using unit cells with three or four representative fibres [14, 15], some others were adopted from polymer network modelling [16], were based on affine structural approaches [17–19], or statistical averaging [20, 21]. While these approaches are beneficial in terms of computational effort, the relation between microscopic properties and macroscopic behaviour is essentially established through specific assumptions. This typically concerns the coupling between fibre and macroscopic kinematics, so that the reliability of the model predictions depends on how well these assumptions are met in real networks. Discrete network models (DNMs), in which single fibres are represented by finite elements (FEs) and their ensemble response to macroscopic loads is computed from the displacements and forces at the boundaries of representative volume elements (RVEs) allow for more details in describing the scale transition. In addition, these models provide access to changes of microstructural properties such as pore and fibre shapes, fibre orientation or inter-fibre interactions upon macroscopic loads. *Vice-versa* these models also reveal the effect of alterations of these quantities on the macroscopic response. DNMs are therefore valuable tools to study general aspects of fibre network mechanics [e.g. 22] and were applied to model, e.g., paper [23–26], glass-fibre felts [27], collagen and other biopolymer networks [28–31], and, finally, ESNs [32–38].

The large planar dimensions and layered structure of electrospun mats compared to their thickness of typically few hundred micrometers motivate the simplification that ESNs can be treated as two-dimensional networks [27, 33, 39, 40]. This reduction poses the need for further assumptions on the number and locations of the points at which fibres would interact through the third dimension. With a focus on this aspect, we have recently presented a planar, sparse and ESN-specific 2.5D DNM, based on the concept of *interaction thickness* that allows distinguishing cross-links from mere fibre intersections by assuming that cross-links only form if fibres are in sufficient out-of-plane proximity [41]. This model, informed only by single fibre material and network geometrical properties showed excellent predictive qualities when compared to mechanical tests on polyamide ESNs [15]. Noteworthy, the reduction to a 2D representation loses applicability when aspects related to the out-of-plane mechanics on scales in or below the order of the network thickness are investigated, for example, solid-fluid interactions at fibre level in filtering applications. Such aspects pose the general need for 3D models.

Independent of the considered dimensionality, the models need to be informed by experimental data on network topology and single fibre characteristics. While the latter can be obtained from single fibre testing [42, 43], information about fibre shape, diameter and orientation distribution can be extracted from scanning electron microscopy (SEM) images [33, 37]. SEM information is, however, restricted to the outer surface of ESNs from which only limited information on three-dimensional features, such as out-of-plane fibre shape or cross-link density, can be retrieved [41]. Due to fibre diameters that may be significantly below 1 µm, also most laboratory 3D imaging techniques such as microCT, do not provide the necessary resolution in general [44], whereas sequential imaging techniques, such as SEM after focused ion beam slicing are time consuming and require a high degree of post processing [45]. Notably, it is exactly the identification of cross-links and associated structural parameters that is essential for a reliable prediction of macroscopic and fibre scale properties, as the mechanical response is strongly affected by the interaction between fibres [41].

In order to circumvent these problems, one may generate the DNM by depositing a set of random fibres in a way inspired by the process of network formation, and identify the cross-links from the simulated fibres that are in contact. Fibre deposition models have been proposed for paper [24, 26, 46], but also for ESNs [34, 38], based on different computational techniques. Using the explicit finite element method (FEM) we present in this contribution a fibre deposition model which aims at a dedicated representation of network formation during the electrospinning process. In these *virtual spinning* simulations, fibres are dropped and accelerated towards a rigid collector plate by a body force, bend upon contact with other fibres, and form a highly porous three-dimensional network. By this means, ESN-specific 3D RVEs are obtained that can be used in subsequent simulations to compute the homogenised mechanical response. The models enable a quantitative evaluation of the influence of topological parameters and fibre properties

on the mechanical properties of ESN mats. In addition, the analysis of the network RVEs provides the structural parameters needed in reduced modelling approaches which are hardly accessible in experiments, in particular the density and location of the fibre contact points at which cross-links may form and interactions take place. The 3D model is thus applied to inform a 2.5D efficient ESN representation [41]. After a description of the computational deposition process, we start from identical sets of fibres, from which both 3D and 2.5D RVEs are generated. Missing information in the latter approach is extracted from the former, and used to investigate the assumptions inherent to the interaction thickness concept employed by the 2.5D approach. From both models, the homogenised network responses to macroscopic plane stress load cases are computed and compared, and applicability limits of the 2.5D approach are investigated and discussed.

2. Generation of 3D ESN RVEs and associated mechanical analysis

In this section, a numerical framework to create models of ESNs is presented. The method is inspired by the process through which non-woven random networks form from extremely long fibres during electrospinning. In particular, fibres of given planar geometry are discretised by finite beam elements and deposited to form three-dimensional RVEs. Macroscopic deformations are imposed through corresponding boundary conditions in a subsequent step, in order to compute the homogenised network response.

2.1. Description of fibre shape

In addition to the base material from which the fibre is spun, its shape obtained while solidifying and falling during the electrospinning process represents an important characteristic of the fibre. While fibre formation is a complex process during electrospinning, the final shape of fibres within the network, or at least their planar projection, is amenable by microscopy analysis [14, 33, 37, 39], and can be described as a curve in two or three dimensions. In order to represent these curves mathematically, both deterministic and stochastic methods can be used.

Deterministic shapes predefine the fibre path completely based on a finite set of parameters. Examples are, e.g., a straight line (Fig. 1b) or truncated Fourier series of the form

$$\eta(\xi) = \sum_{k=1}^{n} \alpha_k \sin\left(\frac{2\pi\xi}{\Lambda_k}\right) + \beta_k \cos\left(\frac{2\pi\xi}{\Lambda_k}\right) \tag{1}$$

that represents a periodic function in the ξ-η-plane, parametrised with respect to the linear coordinate ξ along a direction specified by a unit vector $\boldsymbol{R}$ (Fig. 1a). For $n = 1, \beta_1 = 0$ this reduces to the special case of sine-shaped fibres [41], where the shape is controlled by the amplitude $\alpha_1 = \alpha_\mathrm{F}$ and wavelength $\Lambda_1 = \Lambda_\mathrm{F}$ (Fig. 1acd). Clearly, straight fibres (Fig. 1b) are included for $\alpha_\mathrm{F} = 0$.

Stochastic fibre shapes can be obtained by random-walk algorithms, where a succession of points produced by the algorithm is connected with straight lines or splines [47–49]. Here, we propose to describe the shape of electrospun fibres by the statistics of worm-like chains [50–52], characterised by the persistence length ℓ that quantifies the correlation between the angle $\theta(s)$ formed between tangent vectors to the chain at positions separated by a distance s along the chain contour. For a planar, i.e. two-dimensional worm-like chain the correlation is given by the Gaussian probability density [52]

$$\mathcal{P}(\theta(s)) = \sqrt{\frac{\ell}{2\pi s}} e^{-\frac{\ell\theta^2}{2s}} \tag{2}$$

with the standard deviation σ_θ

$$\sigma_\theta = \sqrt{\frac{s}{\ell}}. \tag{3}$$

Compared to other stochastic fibre models, the worm-like chain model comes with the advantage that the persistence length ℓ can be estimated from images [53], as shown for, e.g., DNA [54], microtubules [55] and collagen fibres [56]. Once ℓ and the orientation $\boldsymbol{t}_0$ of one segment is defined, the fibres are generated by consecutively appending segments of length l. The angle θ between two consecutive segments (Fig. 1a) is drawn randomly from a Gaussian distribution with zero mean and standard deviation $\sigma_\theta = \sqrt{l/\ell}$ according to Eq. (3) [52]. Hence, fibre shape is exclusively controlled by ℓ (Fig. 1ef), including straight fibres for the limit $\ell \to \infty$ (Fig. 1b). Noteworthy, due to the

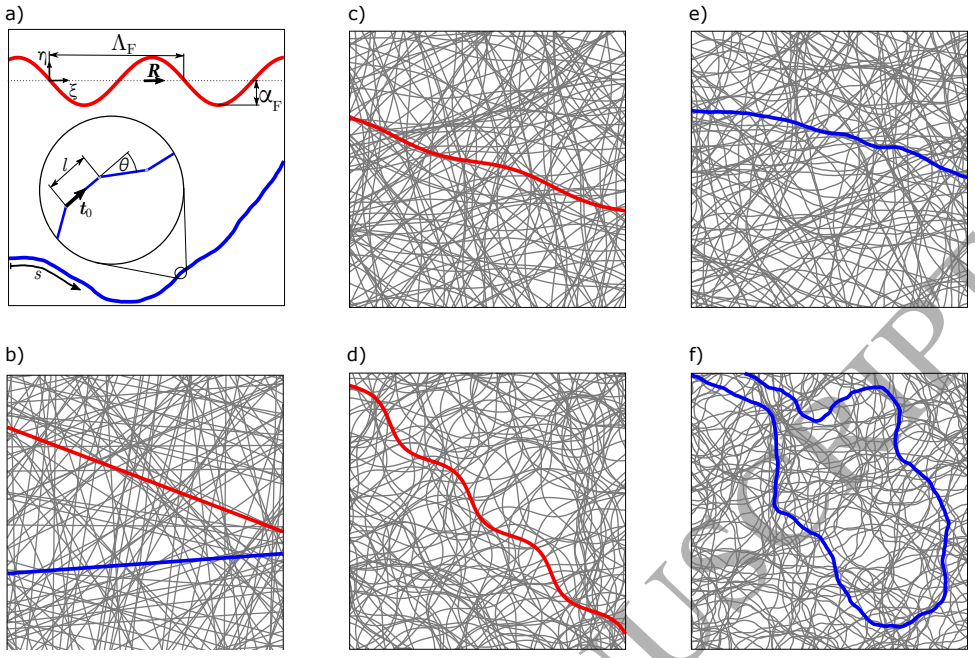

Figure 1: Planar fibre networks with different fibre shapes. **a)** Sinusoidal (red) and stochastic worm-like (blue) fibre shape with associated parameters. **b)** Straight fibres, achievable with $\alpha_F = 0$ and $\ell \to \infty$ for sinusoidal or worm-like fibres, respectively. **c,d)** Sinusoidal fibres with different wavelength Λ_F and amplitude α_F. **e,f)** Stochastic fibres with different persistence length ℓ.

properties of the Gaussian function [e.g. 57, sec. 34], the mean end-to-end vector of a fibre is thus predefined by $\boldsymbol{t}_0$. This property therefore allows the generation of networks with non-uniform orientation distribution by sampling the orientation of the first segment $\boldsymbol{t}_0$ of the random walk from the desired distribution (cf. Carleton et al. [40, 48]). Each fibre is attributed a fibre diameter d_F, either defined from a normal distribution with mean $\bar{d}_F$ and standard deviation σ_{d_F}, or set constant (e.g. $d_F = \bar{d}_F$, $\sigma_{d_F} = 0$). The left tail of the normal distribution further needs to be trimmed at $d_{F,min} = \bar{d}_F - r\sigma_{d_F}$ to exclude negative fibre diameters, where r is a positive constant.

2.2. *Virtual spinning: generation of 3D RVEs*

Using Matlab (R2016b, The MathWorks Inc., Natick, MA, USA), sets of N_F fibres with deterministic or stochastic shapes are generated, and distributed randomly in position and orientation within a planar square region of size $b_N \times b_N$, where b_N determines the size of the RVE in the x-y plane (Fig. 2a). The fibres only terminate on the RVE boundaries so that a fibre is always connecting two boundary edges of the RVE. This and all following operations are performed by executing custom Python scripts (2.7.3, Python Software Foundation, OR, USA) using the scripting module of the FE modelling software (Abaqus/CAE 2016, Dassault Systèmes Simulia Corp., Johnston, RI, USA). Initially, each fibre $i \in [1, N_F]$ is placed in a separate plane with offset $z = z_i = d_{F,1}/2 + \sum_{k=1}^{i-1}(d_{F,k} + d_{F,k+1})/2$ from, and parallel to the collector plane at $z = 0$ (Fig. 2a).

Fibres are discretised with Timoshenko beam elements (B31) with an element length of $3d_F$, while the collector plane is defined by a rigid surface. In a dynamic explicit FE simulation (Abaqus/Explicit 2016, Dassault Systèmes Simulia Corp., Johnston, RI, USA), the stack of fibres is successively compacted to create the 3D RVE. To this end, the fibres, initially at rest, are accelerated towards the collector plate by a defined body force $\boldsymbol{g} = -g\boldsymbol{e}_z$ (Fig. 2a). This is similar to the fibre attraction by the collector due to electrostatic forces in the electrospinning process, and the magnitude g was found to correlate with the network porosity. In particular, higher forces cause stronger compaction of the fibre network and therefore lower porosities. To avoid lateral drift, the in-plane displacement degrees of freedom of the boundary nodes of each fibre are fixed during the falling process. The interaction between individual fibres, and between fibres and collector is modelled as hard, frictionless contact, enforced with the penalty stiffness algorithm

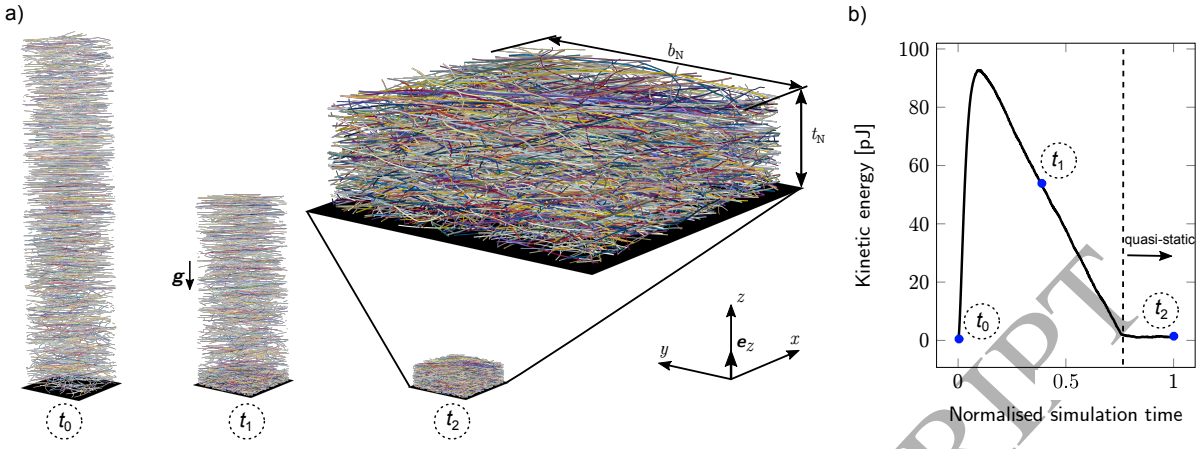

Figure 2: **a)** Reference t_0, intermediate t_1 and final t_2 configuration of the virtual spinning process. ($N_F = 1600$, $b_N = 300\bar{d}_F$) **b)** Kinetic energy during the virtual spinning simulation. The quasi-static solution was reached when the kinetic energy reached a constant, negligible value.

implemented in the FE software which accounts for the fibre diameter [58]. At this stage the fibre material is modelled as linear elastic with Young's modulus E_F and Poisson's ratio ν_F, furthermore a mass density ρ_F is assigned. Mass proportional Rayleigh damping is introduced to allow the dynamic dropping process to reach the quasi-static solution state, i.e the compacted electrospun network geometry. For this type of damping (controlled by a damping factor α_R), the damping forces are proportional to the absolute velocity at the nodes, which reflects the idea of dissipation due to interaction between fibres and the surrounding, aeriform fluid in the electrospinning chamber. A constant time step Δt is chosen whereas the stability of the integration is ensured by mass scaling [27]. The system is considered at rest when the kinetic energy of the system drops below one percent of the maximal value (Fig. 2b). The corresponding state is considered as the quasi-static solution of the problem and the deformed mesh is stored to provide the final geometry of the RVE.

2.3. Extraction of network parameters

In a post-processing step, the locations of contact between fibres are identified, corresponding nodes are determined, and finally contact pairs and associated fibres are stored for further post-processing. The thickness t_N is determined from the so created RVE by sampling the maximal distance of fibre material from the ground collector within each subdomain defined by a regular in-plane grid with grid size $0.1b_N \times 0.1b_N$ and finally averaging over all subdomains. The RVE volume is thus given by $V_N = t_N b_N^2$. The volume of all finite elements provides the total fibre volume V_F, so that the fibre volume fraction ν and network porosity ϕ are given through

$$\phi = 1 - \nu = 1 - \frac{V_F}{V_N}. \tag{4}$$

While the RVE geometry can be used for the 3D analysis of the mechanical response of the network as described in the next section, it furthermore enables the structural analysis to extract topological features that are difficult to access experimentally, such as the cross-link density or pairs of fibres in contact (see Fig. 7a). The identification of cross-links is based on the 3D topology of the networks and therefore allows distinguishing between real contact points and projected fibre intersections, in contrast to image based methods. This is highlighted in Fig. 3b, which shows a rendered image of the 3D network with one single fibre and the identified contact points coloured in blue and red, respectively. The image reveals how difficult it is to distinguish projected intersections from actual fibre contact points by visual inspection. Moreover, the lengths l_s of all fibre segments are identified, defined as the contour length of a fibre segment between two cross-links, and the corresponding distribution with mean $\bar{l}_s$ is evaluated (Fig. 7c). The evaluation of average segment length indicates a dependence on the z-position (Fig. 3a), with higher segment lengths near the lower and upper network surface. This results from the decreasing probability for cross-link formation at the surfaces (cf. also Zündel et al. [41]), and the asymmetry between bottom and top is induced by the slightly higher

compaction of the fibres close to the the collector plate. These findings highlight that the network properties at the visually accessible surfaces may not be representative for the bulk of the material.

2.4. Computation of homogenised RVE response

The RVEs generated according to Sec. 2.2 are used as stress-free reference configurations for further mechanical computations in Abaqus/Explicit, allowing the extraction of the homogenised stress response of the network at the macroscopic and the associated kinematics at the microscopic scale (Fig. 5). To this end, the macroscopic state of deformation is imposed by homogeneous displacement boundary conditions at the lateral boundary faces of the RVE, while the top and bottom surface are unconstrained, assuming a macroscopic state of plane stress in the fibre mats. Traction free lateral faces, such as in uniaxial extension with lateral contraction, are realised by coupling the lateral degrees of freedom of the boundary nodes and requiring that the overall traction on each of these faces vanishes [29]. The single fibre material is modelled with a linear elasto-plastic material law, defined by Young's modulus E_F, Poisson's ratio ν_F, yield stress $\sigma_\mathrm{F}^\mathrm{p}$ and post-yield slope K_F^p, capturing the typical elasto-plastic single fibre response with a small, approximately linear elastic regime common for electrospun polymers [43, 59, 60]. To simulate the presence of permanent cross-links between fibres at the identified locations of interaction (Sec. 2.2) the translational degrees of freedom of the corresponding adjacent nodes of the fibres in contact after the fibre deposition process are coupled. Notwithstanding this simple choice made here, more involved fibre material laws and, once the locations of contact have been identified, other interaction laws can be implemented in a straightforward manner. All evolving mechanical interactions between fibres occurring during the network loading as a result of the RVE deformation are accounted for by frictionless, hard contact using the penalty method as specified in Sec. 2.2. Representative network dimensions have been selected accordingly to preceding convergence studies (see Appendix A). The boundary value problem was solved through explicit FE analysis, suggesting some advantages when simulating discrete fibre systems [27]. In particular, explicit time integration was able to robustly handle the large number of evolving contacts between fibres, and the rapid changes in fibre configurations due to bending, and buckling instabilities. To ensure that the kinetic energy is negligible and the solution can be considered quasi-static, the maximal rate of applied strain was restricted (here $\dot{\varepsilon} = 0.015\%/s$). Slight Rayleigh damping (α_R) is considered and the stability of the explicit time integration is ensured by mass scaling for the specific time step Δt. To verify the chosen values for $\dot{\varepsilon}, \alpha_\mathrm{R}$ and Δt a representative simulation was conducted three more times where for every simulation one of the parameters was reduced to its half (see Appendix A). No significant difference could be observed.
In a post-processing step, based on custom Python scripts, the volume averaged first Piola-Kirchhoff stress tensor is

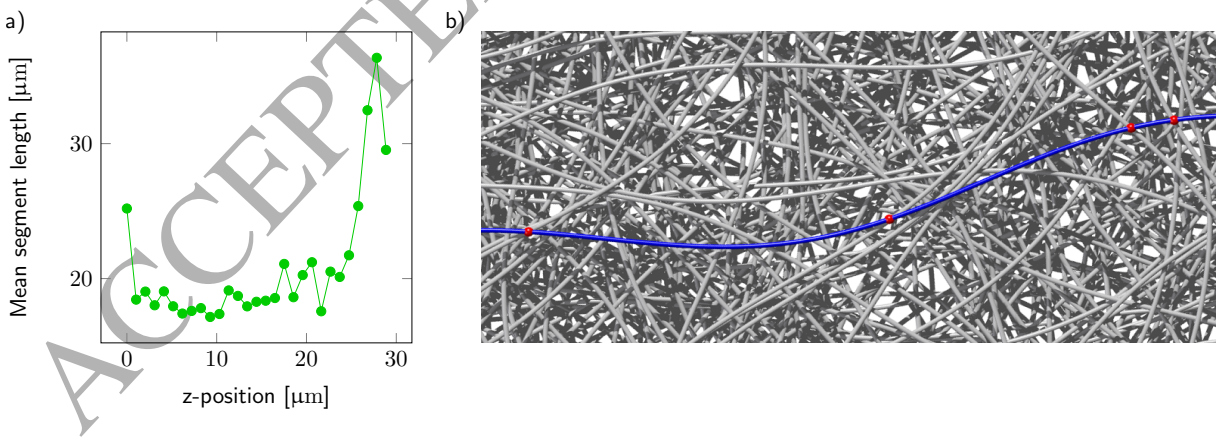

Figure 3: **a)** Dependence of mean segment length on the z-position within the network, evaluated in network intervals $\Delta z = 1\mu$m. **b)** Graphical visualisation of the model (top view), demonstrating for a single fibre (blue) the difficulty to distinguish contact points between fibres (red) from mere visual intersections related to the projection of the 3D model to a 2D image.

1.) Define RVE in-plane dimension $b_\mathrm{N} \times b_\mathrm{N}$ and number of fibres N_F.
2.) Generate N_F randomly distributed fibres in the plane of the RVE.
IF *fibre shape* = periodic deterministic **THEN**
Define $\alpha_k, \beta_k, \Lambda_k$ as input parameters.
Generate in-plane fibre shape according to Eq. (1).
ELSEIF *fibre shape* = stochastic **THEN**
Define persistence length ℓ as input parameter and choose step length l ($l \ll \ell$).
Generate in-plane fibre shape by a random walk where the angles θ between steps are sampled from a Gaussian distribution with zero mean and standard deviation $\sigma_\theta = \sqrt{l/\ell}$.
ELSE
Generate straight fibres.
END
3.) Stack fibres in the out-of-plane direction on to each other and assign fibre material and contact properties.
4.) Do virtual spinning simulation (Sec. 2.2) to compact network.
5.) Extract topological information (Sec. 2.3), e.g., contact points, segment length l_s, porosity ϕ.
6.) Import final mesh as reference configuration for a second simulation, where load case specific boundary conditions are applied (Sec. 2.4). Assign fibre material and contact properties. Couple degrees of freedom of initial contact nodes.
7.) Solve boundary value problem (Sec. 2.4) and compute homogenised material response (Eq. (5)).

Figure 4: Algorithmic box describing the general steps for the generation and homogenisation of 3D RVEs.

calculated from the nodal forces $\boldsymbol{f}_i$ and reference positions $\boldsymbol{X}_i$

$$\mathbf{P} = \frac{1}{V_\mathrm{N}} \sum_{i}^{N_\mathrm{b}} \boldsymbol{f}_i \otimes \boldsymbol{X}_i \tag{5}$$

of all boundary nodes $i = 1, 2..., N_\mathrm{b}$ [33].

3. Comparison with the reduced 2.5D model

The 3D RVEs generated through the explicit fibre deposition process (Sec. 2) were used to inform a recently proposed reduced 2.5D modelling approach [41] and validate a key assumption of this model on the out-of-plane interaction between fibres. To this end, topological information extracted from the 3D RVE was used to define model parameters of the 2.5D approach, and the mechanical response predicted by the full and reduced modelling approaches were compared. Finally, a scaling law between porosity and cross-link density, revealed from computational analyses based on the 3D model, was used to further reduce the number of parameters in the 2.5D approach.

3.1. Reduced 2.5D modelling approach

The reduced modelling approach used here was presented previously [41] and is specific to electrospun networks, allowing the generation of planar RVEs, and featuring a physically motivated definition of fibre cross-links. Briefly, the algorithm takes into account that the RVE grows in thickness with every deposited fibre, and that fibre intersections appearing in the planar projection of the network can only form a cross-link if the two intersecting fibres are effectively in contact. The latter condition is implemented by associating an out-of-plane position z to each fibre, and assuming that a fibre can form cross-links with other fibres only within a layer of a specified interaction thickness t_I. It can be shown that the latter is directly related to the average segment length $\bar{l}_\mathrm{s}$ in the network [41]. It is important to note that the RVEs are essentially two-dimensional, and that the interaction thickness is only a concept to distinguish between intersections and cross-links in the sparse planar network.

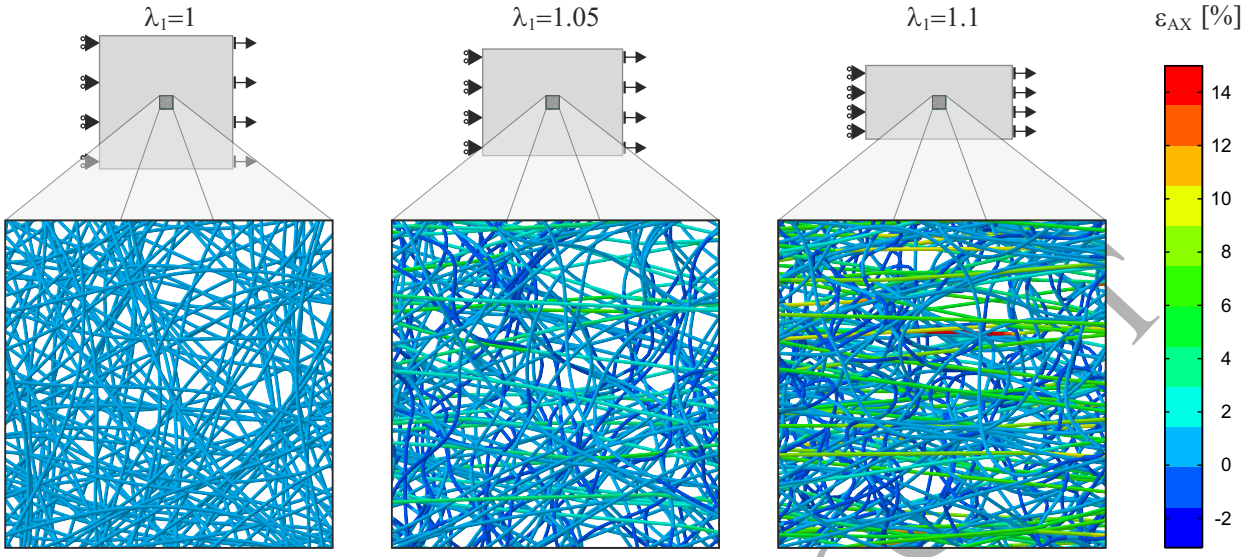

Figure 5: Close up of local fibre deformation for three different states of uniaxial extension with lateral contraction. Colors refer to axial strains ε_{AX} of the beam elements.

In addition to either t_l or $\bar{l}_s$, the network porosity ϕ, and the fibre shape and material properties need to be defined. The former is given by a sine-shape with α_F and Λ_F according to Sec. 2.1 and a constant fibre diameter d_F. The latter are defined through a linear elastic-plastic constitutive law, equivalent to the fibre material in the 3D approach (E_F, ν_F, σ_F^p, K_F^p). Boundary value problems are defined through imposed homogeneous displacement boundary conditions on the lateral edges of the planar RVEs, solved by implicit 2D FE computations (Abaqus/Standard, Version 6.10-EF1, Dassault Systmes Simulia Corp., Johnston, RI, USA), and the homogenised stresses are computed according to Eq. (5).

Noteworthy, in addition to employing an implicit solver, the reduced model [41] differs from the full 3D approach in that it disregards any out-of-plane motion, and does not account for the additional contacts between fibres that may result from their motion. Moreover the reduced model needs information about both the porosity ϕ and average segment length $\bar{l}_s$ of the network, while these two parameters are strictly related in the 3D generation approach, since higher compaction of the network during the virtual spinning process leads to both a reduction of porosity and segment length at the same time. Based on a set of test cases defined in the next section, the effect of these differences on the prediction of the microscopic fibre kinematics and the homogenised network response was investigated.

3.2. A set of test cases

Equivalent RVEs for the 3D and 2.5D approach, respectively, were generated according to the following procedure (Fig. 6): At first, a set of fibres with random orientation was generated. Next, 3D RVEs were generated as described in Sec. 2.2, and porosity and average segment length were extracted (Sec. 2.3). Based on this information, 2.5D RVEs were generated from the same stack of fibres. Finally, both RVEs were then used to simulate macroscopic uniaxial tension, strip-biaxial and equibiaxial extension tests, and their homogenised responses were compared.

Specifically, fibres were modelled with sine-shape ($\alpha_F = 7\mu m$, $\Lambda_F = 150\mu m$) and constant circular cross-section ($d_F = 1\mu m$), and the mass density of the fibre material was set to $\rho = 0.9 g/cm^3$. Their constitutive behaviour was defined by a linear elastic-plastic material law with Young's modulus $E_F = 1500MPa$, Poisson's ratio $\nu_F = 0.4$, yield stress $\sigma_F^p = 30MPa$, and post-yield hardening parameter $K_F^p = 150MPa$. With this parameter set, and by adjusting the mass specific body force g, RVEs with a porosity of $\phi = 0.965$ and an average segment length of $\bar{l}_s = 19.7\mu m$ were generated (both values are average values of $N = 3$ realisations of the RVEs). An RVE size of $300\mu m \times 300\mu m \times 28.3\mu m$ ($b_N \times b_N \times t_N$) was selected in line with a convergence study performed beforehand (Appendix A).

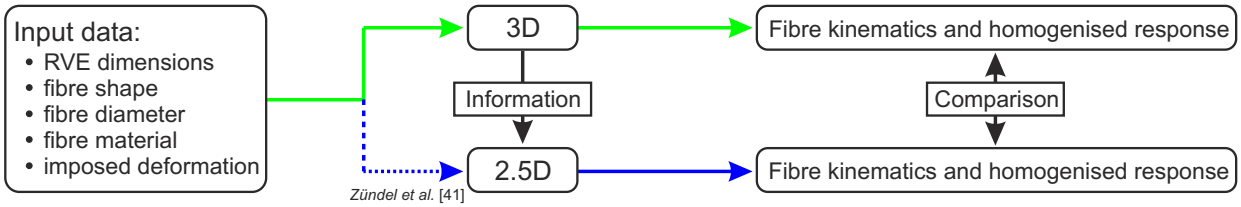

Figure 6: Procedure for comparison between 2.5D and 3D modelling approaches

3.3. *Validation of the interaction thickness concept*

Besides the shape and mechanical behaviour of single fibres, the mechanical response of a network-like structure is strongly affected by the location and density of cross-links between the fibres. The cross-link density correlates directly with the mean length of fibre segments $\bar{l}_s$, i.e. the contour lengths of fibre sections between cross-links.

As mentioned, the reduced approach [41] requires either $\bar{l}_s$ or the interaction thickness parameter t_I to be defined. Generating networks with a given t_I according to this approach (Sec. 3.1) and sequentially indexing the fibres by their initial vertical position in the stack from bottom to top, one obtains an interaction matrix by entering a marker for each pair of fibres i and j, $i, j, = 1, 2, ..., N_F$ that are in contact (blue dots in Fig. 7a). The constant t_I constrains the markers to a narrow band.

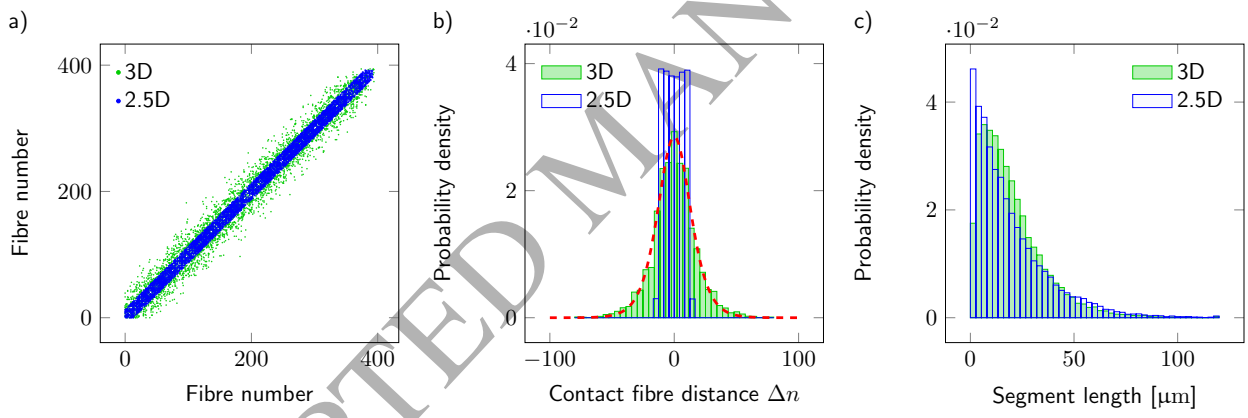

Figure 7: **a)** Connectivity matrix of the networks, representing graphically the fibres that are connected by cross-links. The fibres are numbered by their order of deposition. Data is shown for one representative network. **b)** Histogram of the difference of indices $\Delta n = i - j$ of fibres in falling order shared by a contact. Data extracted from $N = 3$ networks for the 3D and 2.5D case, respectively. **c)** Histogram of the segment lengths l_s. Data extracted from $N = 3$ networks for the 3D and 2.5D case, respectively.

The analysis of fibre connectivity extracted from the equivalent 3D RVEs reveals that the out-of-plane interaction of the fibres is indeed limited (Fig. 7a, green markers), however, less sharply bounded than assumed by the reduced approach. The information contained in the connectivity chart can also be represented as probability distribution of the difference $\Delta n = (i - j)$ of the fibre indices that share a cross-link. For the reduced approach this results in a homogeneous distribution within the interaction layer and zero cross-link formation probability outside, while the probability distribution describing the 3D RVEs shows that only a part of the cross-links (~61%) are formed within this range (Fig. 7b). In fact, these networks also form cross-links with fibres that were more distant in out-of-plane direction, albeit with decreasing probability. For the analysed networks, the latter distribution was well captured by a logistic probability density function

$$\mathcal{P}(\Delta n) = \frac{e^{\Delta n/s}}{s\left(1 + e^{\Delta n/s}\right)^2} \tag{6}$$

with zero mean and shape parameter $s = 8.775$ ($R^2 = 0.99$), where Δn was considered a continuous parameter here. Hence, the results provided by the 3D model clearly confirm that the probability of cross-link formation between fibres is governed by their out-of-plane proximity, and therefore support the concept of an interaction layer, even if the boundaries are less well defined than assumed in the reduced 2.5D approach.

While for the present comparison, cross-link density and hence mean segment length were equal for both approaches by definition, the distributions of segment lengths differ (Fig. 7c). The main difference occurs for short fibre segments ($l_s < 5\mu m = 5d_F$), for which the 3D RVEs reveal a decreasing probability density in contrast to the reduced approach. This difference is explained by the method of identifying potential cross-links in the reduced approach, which is based on searching projected intersections within the interaction layer. This search is based on 1D lines in a 2D space, and does not account for the fibre diameter and bending stiffness. The probability for segment lengths in the order of the fibre diameter or lower is thus higher compared to the 3D approach that accounts for the finite fibre volume and bending stiffness.

3.4. Comparison of homogenised mechanical and fibre kinematic responses

The homogenised mechanical behaviour of the two modelling approaches was compared in terms of their responses to uniaxial (UA), strip biaxial (SB) and equibiaxial (EB) loads, imposed through homogeneous boundary conditions that provide nominal tensile stretches up to $\lambda = 1.15$. For both approaches $N = 3$ RVEs were realised, and

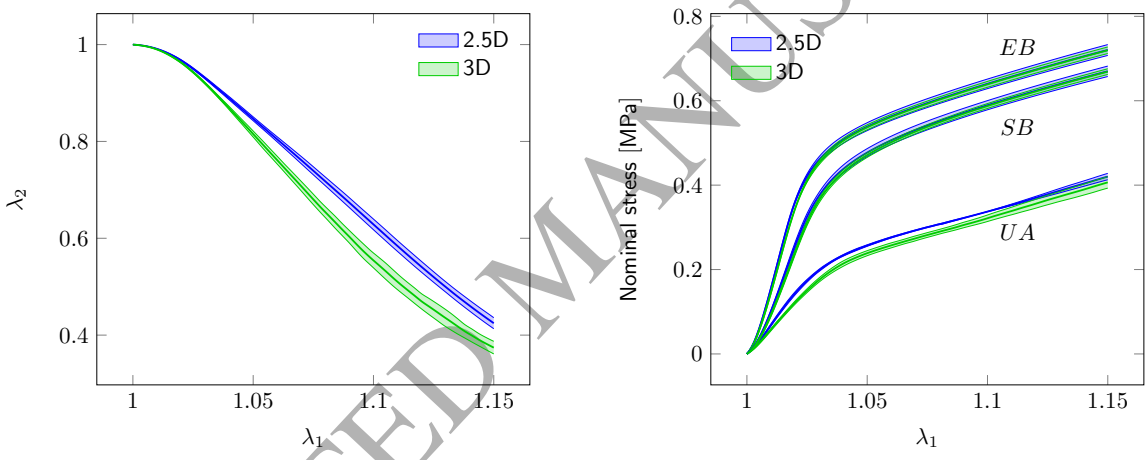

Figure 8: Comparison of macroscopic kinematic and stress response to different loading conditions predicted by the 2.5D and 3D approach, respectively. Results are shown as mean (solid line) and standard deviation (shaded area) for $N = 3$ equivalent networks.

the mean and standard deviation were calculated from their responses (Fig. 8). The results presented in Fig. 8b show that the stress responses predicted by the two approaches match very closely both in the elastic and plastic regime for all three loading conditions. Only for uniaxial tension, the reduced approach slightly overestimates the network stiffness, and underestimates the lateral contraction (Fig. 8a).

While the 2.5D and 3D RVEs differ in terms of the probability of cross-link formation and segment length distribution (Fig. 7), the sound agreement of the macroscopic stress response indicates that the reduced approach captures the mechanisms that are relevant for the macroscopic in-plane mechanical response of such networks. The underestimation of the lateral contraction in the uniaxial tension response can be explained by the difference in the segment length distributions (Fig. 7c), since the lateral contraction behaviour of these networks is strongly related to the slenderness of the fibre segments: The higher density of very short, and slightly lower density of medium sized segments in the 2.5D RVEs leads to an increased resistance to lateral contraction of the fibrous networks, due to their higher resistance to bending and buckling. Furthermore, the restriction to in-plane buckling constrains the possible modes of fibre motion and contributes to the resistance against lateral contraction [61]. These conclusions are backed by the quantitative analysis of the micro-scale kinematics of the networks in terms of orientation and stretch ratio of the segments' end-to-end vectors. Fig. 9 indicates a higher degree of fibre reorientation under loading in the 3D model

(Fig. 9a) as well as a higher amount of compressed fibre segments, i.e. with segment stretch less than one (Fig. 9b). Additionally the reduced approach by definition neglects the out-of-plane kinematics while it can be extracted from the 3D model through the analysis of the out-of-plane fibre reorientation (Fig. 9c).

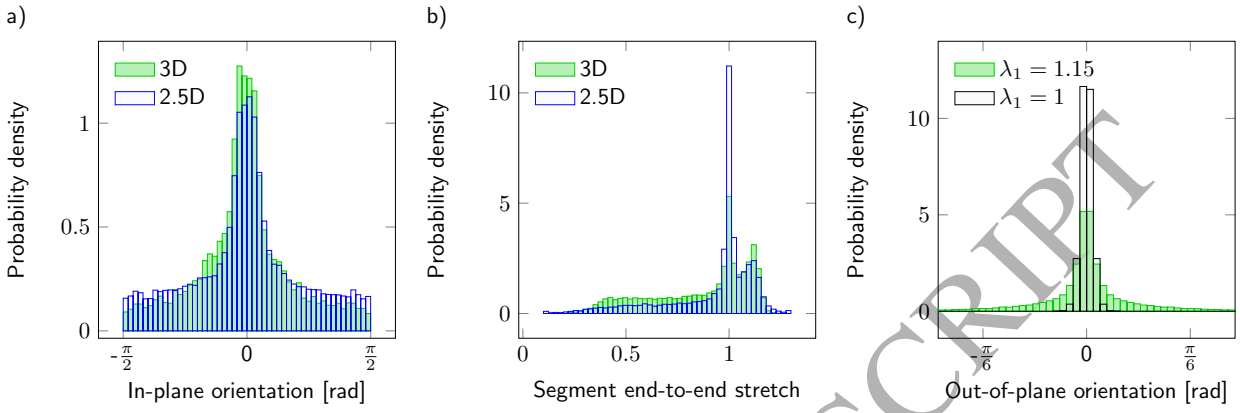

Figure 9: Comparison of in-plane fibre segment orientation (**a**) and segment stretch (**b**) distributions for uniaxial loading ($\lambda_1 = 1.15$) predicted by the 2.5D and 3D approaches, respectively. **c**) Out-of-plane fibre orientation distributions extracted from the 3D model in unloaded and loaded (UA, $\lambda_1 = 1.15$) state. All results are reported for $N = 3$ equivalent networks.

3.5. Networks with distributed fibre diameters

Being the product of a stochastic process, the topological parameters of real ESNs are generally not uniform but characterised by probability distributions. This also applies to the fibre diameter, which varies both along a single fibre and between different fibres as can be noticed from SEM images [62]. This kind of images are usually also employed to quantify ESN fibre diameters, and the data are typically reported as mean diameter and standard deviation ([cf. 63]).

Here we exploit the capability of the 3D virtual spinning approach to account for distributed fibre diameters in the generation of RVEs and examine the effect on the homogenised network response. To this end, networks with normally distributed fibre diameters around the mean $\bar{d}_\mathrm{F} = 1\,\mu\mathrm{m}$ and different standard deviations $\sigma_{\mathrm{d_F}} = [0\mu\mathrm{m}, 0.2\mu\mathrm{m}, 0.45\mu\mathrm{m}]$ were generated and their mechanical responses were compared to equivalent networks generated with the 2.5D approach, which assumes constant fibre diameter equal to the mean. Since the normal distribution is unbounded, the left tail of the fibre diameter distribution was cut at $d_{\mathrm{F,min}} = (\bar{d}_\mathrm{F} - 2\sigma_{\mathrm{d_F}})$ during the network generation, which in our cases was sufficient to avoid negative fibre diameters.

The results of this investigation, presented in Fig. 10, indicate that the increasing standard deviation $\sigma_{\mathrm{d_F}}$ of the fibre diameter has a stronger effect on the lateral contraction than on the stress response. The lateral contraction decreases when the standard deviation $\sigma_{\mathrm{d_F}}$ increases, which is explained by the presence of thicker fibres with increased resistance to bending. More precisely, the bending stiffness of the fibres is determined by their second moment of area, which scales with $\propto d_\mathrm{F}^4$ for circular fibre cross sections. Due to this non-linear dependence, the average bending stiffness of the distributed networks is higher than the bending stiffness of fibres with constant fibre diameter. This also provides an explanation for the lower sensitivity of the stress response on the width of the distribution, as the stress is more strongly affected by tensile fibre stiffness, which is proportional to the fibres' cross section area and therefore only scales as $\propto d_\mathrm{F}^2$.

3.6. Parameter reduction of 2.5D approach

While in the reduced 2.5D approach the network porosity ϕ and average segment length $\bar{l}_\mathrm{s}$ are independent parameters, they are inherently linked in the 3D approach, and finally controlled by the body force g that attracts the fibres towards the collector plate. By tuning this force, a set of networks was generated with porosities $\phi \in [0.83, 0.96]$, which is a relevant range for ESNs [64]. The analysis of the mean segment length $\bar{l}_\mathrm{s}$ extracted from the virtually spun RVEs confirms that the number of cross-links decreases with increasing porosity, leading to a larger $\bar{l}_\mathrm{s}$ (Fig. 11a).

Based on computer simulations of the compaction fibrous networks, Durville [49] suggested that the relation between fibre volume fraction $\nu = 1 - \phi$ and cross-link density n_C in fibrous networks is governed by the power law

$$n_C \propto \nu^{2/3}. \tag{7}$$

Considering that the cross-link density and the average segment length are inversely proportional to each other ($\bar{l}_s \propto n_C^{-1}$), this relation can be rewritten as

$$\bar{l}_s = C\nu^{-2/3} = C(1-\phi)^{-2/3}, \tag{8}$$

where C is a parameter dependent on fibre diameter and shape. We found that this relation also applies to electrospun networks and identified C by fitting for our specific network topology (dashed red line in Fig. 11a). By establishing a closed relation between $\bar{l}_s$ and ϕ, Eq. (8) allows eliminating one free parameter in the reduced approach. In fact, to identify the parameter C for a certain fibre diameter and shape, only one point on the curve in Fig. 11a needs to be known, e.g. from a corresponding 3D RVE.

In the present case, C=2.03μm was found (R^2=0.99) and 2.5D RVEs were created for a set of porosities $\phi \in [0.83, 0.96]$ with $\bar{l}_s$ determined by Eq. (8). The predicted responses in uniaxial tension were compared to those of the corresponding 3D RVEs in terms of the slope of the stress-stretch curve (~elastic modulus) and approximated Poisson's ratio, determined from the secant slope of the $P_{11} - \lambda_1$ and $\lambda_2 - \lambda_1$ curves at $\lambda_1 = 1.01$. These results demonstrate that the reduced approach captures well the initial lateral contraction behaviour over the analysed range of porosities (Fig. 11c). However, the elastic modulus of the 2.5D RVEs starts to deviate significantly for porosities $\phi < 0.9$ towards a stiffer response (Fig. 11b).

We hypothesized that this overestimation is due to the inability of the planar model to account for the increasing out-of-plane curvature of the fibres at low porosities. To illustrate this, the out-of-plane angle φ of fibre segments was extracted from the 3D RVEs. An example of their distribution is shown in Fig. 12a, for a high and low porosity, respectively. Describing the probability density by a von Mises distribution

$$\mathcal{P}(\varphi) = \frac{e^{\kappa\cos(\varphi)}}{2\pi I_0(\kappa)}, \tag{9}$$

the concentration parameter κ of the fitted distributions ($R^2 > 0.98$ for all cases) reveals the increasing concentration of the fibre segments onto a plane with increasing porosity, as shown in Fig. 12b. The marked non-linear increase of κ around $\phi = 0.9$ suggests that beyond this value, fibres are strongly concentrated onto the membrane plane which may justify the assumption of quasi-planarity inherent to the 2D models, which is in line with the deviations observed for the elastic modulus (Fig. 11b).

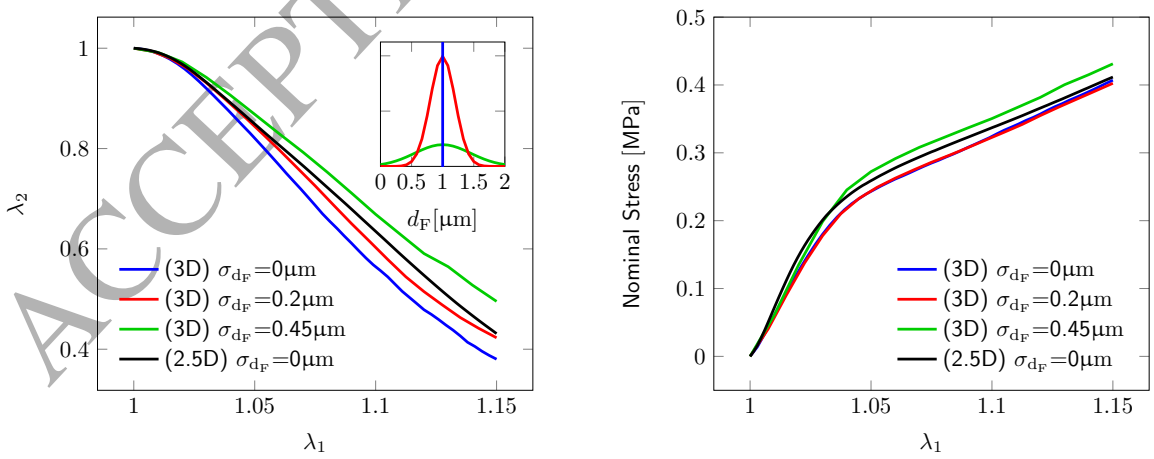

Figure 10: Comparison of kinematic and stress response to uniaxial loading predicted with the 2.5D approach with constant diameter (d_F = 1µm) and with the 3D approach, with diameters sampled from a Gaussian distribution (illustrated in the inset) with mean $\bar{d}_F$ = 1µm and standard deviation σ_{d_F} as specified in the legend.

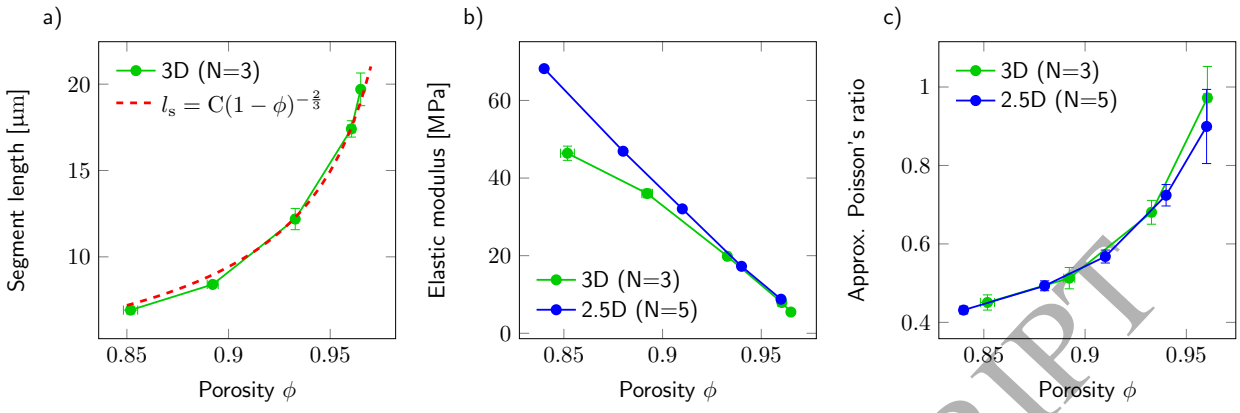

Figure 11: **a**) Fit of Eq. (8) to values generated by virtual spinning (C=2.03µm, R^2 = 0.99) **bc)** Values of the elastic modulus (**b**) and the approximated Poisson's ratio (**c**) evaluated as secant slopes of the $P_{11} - \lambda_1$ and $\lambda_2 - \lambda_1$ curves, respectively, for uniaxial tension at $\lambda_1 = 1.01$.

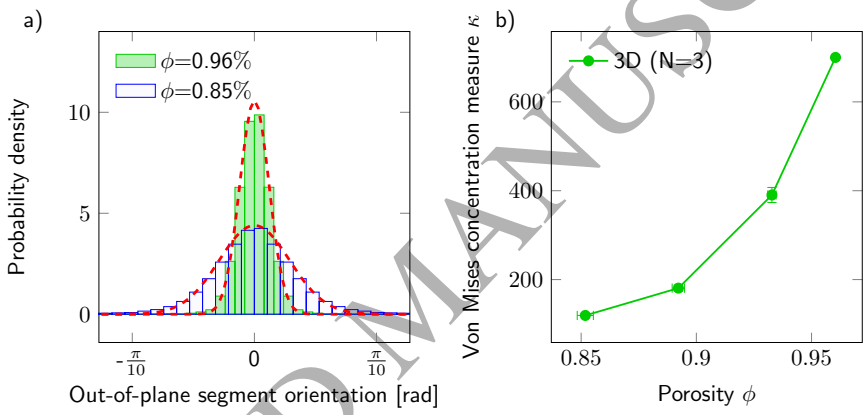

Figure 12: **a)** Histogram and von Mises distribution fit of the out-of-plane segment orientation distribution for two networks with distinct porosities ϕ generated by the virtual spinning approach. **b)** Concentration parameter κ of the von Mises distribution fit (R^2>0.98 for all cases) to the out-of-plane segment orientation for different porosities ϕ. Values are given as mean and standard deviation (error bars).

4. Discussion and conclusions

In order to investigate the relation between topology, micromechanical deformation mechanisms and macroscopic mechanical behaviour in ESNs, a three-dimensional, FE based discrete network model is presented in this contribution. Their particular morphology and fibre properties distinguish ESNs from other fibrous materials, thus requiring specific models to analyse their mechanical behaviour at all length scales. Therefore, the proposed generation of RVEs accounts for some essential features of the network formation process, and generates RVEs specific to ESNs, including the large length and substantial slenderness of electrospun fibres, the low tortuosity of the fibre segments, their peculiar layered fibre disposition, and the cross-links of coordination four formed by two continuous fibres, respectively [see e.g. 65]. Additionally, the model is able to account for inter-fibre interactions in terms of both true material cross-links and contact arising during network deformation.

While there is increasing interest in modelling various aspects of electrospun fibre formation and properties [5], there are only few contributions that accounted for the specific three-dimensional structure of ESNs by explicitly modelling the fibre deposition process. Noteworthy however, there are commonalities with network formation in paper making, in spite of the huge differences of the process in general. With application to paper, lattice based methods have been proposed [26, 46] to consider fibre deposition. The essential difference to the method presented herein lies

in that the fibre properties are regarded in a flexibility parameter that controls the out-of-plane inclination of the fibres. In contrast, the finite element discretisation and modelling of the fibres allows to directly account for various fibre properties and the resulting mechanical behaviour during deposition and network assembly. Based on explicit FE simulations such a method was very recently communicated for generating paper-specific networks and studying their fracture behaviour [24]. The final networks were largely obtained by a surface that compacts the fibres at a prescribed speed. In application to ESNs, FE discretised fibres were considered in the work by Liu and Dzenis [38], where fibres were placed in distinct horizontal square planes and finite element methods were used to compute the final network geometry. Different from our work, the network formation was enforced by prescribing the vertical displacement at the fibre ends, pulling them towards to the collector plate while simultaneously accounting for inter-fibre interaction using a contact algorithm. These networks were then used to predict the response in uniaxial extension, where the load transfer between fibres was limited to friction-based contact. Note that the displacement based method to compact the networks in [38] is conceptionally different from the electrospinning process. The use of volume forces as in the molecular dynamics based simulations in [34] seems more appropriate to model the electrostatically driven network assembly. In [34], the fibres are represented as chains of beads and inter-fibre interaction is modelled by a Lennard-Jones potential during compaction and cross-links connect the fibres during the stretching of the generated networks for the prediction of the mechanical response. While the molecular dynamics approach allows interesting insights into the fracture mechanisms of ESNs, the FE based fibre discretisation seems more suitable for the length-scale and physics of the beam-like electrospun fibres. The here presented method combines the FE based fibre discretization approach with the volumetric force driven fibre deposition and is enhanced with additional aspects, such as the possibility to account for different fibre shapes and the ability to compute the homogenised 3D stress response to an arbitrary macroscopic RVE deformation.

The quasi-planar topology of ESNs, i.e. the low out-of-plane reach of the fibres, which is also present in the virtually generated 3D RVEs, is often used as an argument for reduced 2D modelling approaches that usually benefit from an increased computational efficiency [27, 33, 39]. Evidently, the reduction of a 3D geometry to a 2D planar structure implies modelling assumptions, in particular on the number and locations of interactions between fibres. Common imaging techniques such as SEM [39, 66, 67] provide little insight in this regard, since cross-links can hardly be distinguished from mere intersections of the projected fibres [41]. We propose here to close this gap using the potential of a manufacturing inspired 3D model to support and validate assumptions for reduced models. This approach has been illustrated by generating 3D ESN RVEs with the virtual spinning method, and comparing their microscopic topology and kinematics as wells as the macroscopic mechanical behaviour to the one predicted by a reduced 2.5D model, that uses assumptions on cross-link density and distribution [41]. Although the analysis of the spatial distribution of the cross-links within the 3D RVEs generally confirmed the formation of cross-links within a narrow band, (Fig. 7a) the proposed implementation using a uniform probability distribution within the band may be to restrictive. Infact, the analysis of the 3D RVEs suggests a less sharp distribution, spreading cross-links over a wider range (Fig. 7b) and we found that this distribution can be approximated by a logistic probability function, which could be used to enhance the reduced approach.

In order to compare the macroscopic response, the networks were subjected to three different deformation modes. Both the stress responses and the kinematics predicted by the reduced approach showed good agreement for networks with high porosity. This thus largely validates the 2.5D modelling assumptions with respect to fibre planarity and cross-link identification (Fig. 8). For the here presented comparison of the 3D model with a 2.5D model, the translational degrees of freedom at the cross-links were coupled. This is clearly a constitutive assumption as the load transfer at cross-links is difficult to access experimentally. In fact, an additional coupling of the rotational degrees of freedom at the cross-links reduces the lateral contraction in the case of uniaxial extension as illustrated in Fig. 13a. Besides cross-links the 3D computational model accounts for new contacts that form during the deformation process and at which fibres interact. Neglecting these new contacts has a significant effect on network kinematics observed as a decrease of resistance to lateral contraction (Fig. 13b). As seen from Figs. 8 and 13, the 2.5D model is in better agreement with the predictions that include the presence of additional interactions. This suggests that the confinement to in-plane fibre bending modes inherent to the 2.5D model has a similar effect on the lateral contraction as the consideration of additional contacts in the 3D model, albeit being based on a different mechanism.

The analysis of networks with different porosities, reported in Fig. 8 in terms of their linearised, small-strain response to uniaxial tension, revealed an increased deviation of the predicted elastic moduli between the two approaches with decreasing porosity (Fig. 11a). These results indicate a significant overestimation of stiffness by the reduced ap-

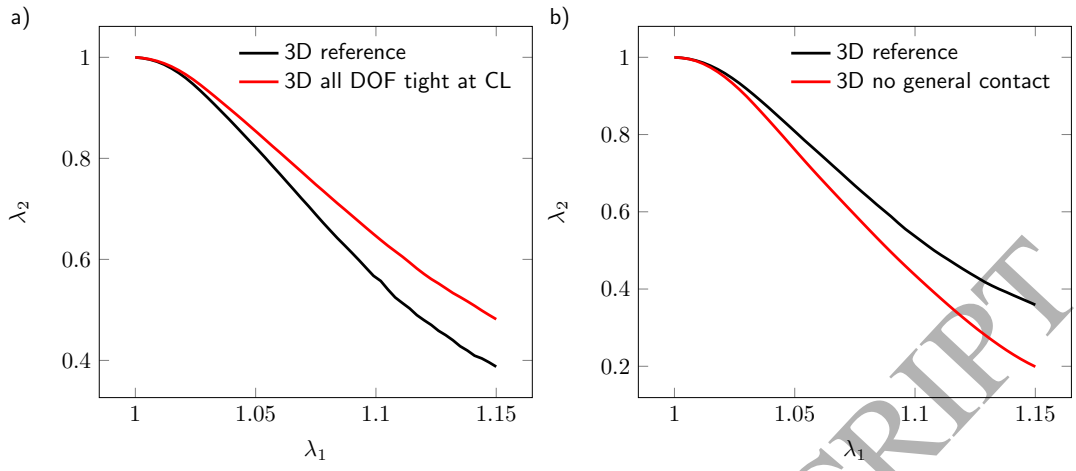

Figure 13: Examples showing the influence of **a**) coupling the rotational degrees of freedom (DOF) at the cross-links (CL) and **b**) neglecting additional fibre interactions (contact) forming during deformation on the macroscopic kinematics predicted by the 3D model for uniaxial loading.

proach for porosities $\phi < 0.9$. This finding highlights the deficiency of planar network models to account for the increasing fibre slackness induced by the out-of-plane curvature (Fig. 12a), which these models neglect by definition. The capability of the 3D approach to handle networks with varying fibre diameters has been used to investigate the assumption of a constant (averaged) fibre diameter, another simplification common to most modelling approaches [32, 33, 37]. In terms of the homogenised stress response this was shown to have a minor effect for the analysed fibre diameter distributions ($\sigma_{d_F} < 0.45$) which reflect the distributions measured in real ESNs (cf. [68]).
Generally, the assumptions used in reduced modelling approaches may add additional modelling parameters. In the case of the reduced approach [41], this led to independent parameters controlling porosity ϕ and average segment length $\bar{l}_s$. The numerical studies performed with the 3D models, suggested that these two parameters are strictly related for a given fibre shape, diameter and mechanical behaviour, and follow a power-law (Eq. 8) reported before for another fibre compaction process [49]. By use of this relation the number of free parameters in the 2.5D approach could be reduced by one.

The main advantage of using reduced 2D modelling approaches is the increase in computational efficiency. For the numerical models used in this study, higher computational costs in the 3D approach were mainly associated with the additional numerical simulation needed to compute the RVE geometry, i.e. the virtual spinning. The associated computational time was about one order of magnitude higher than that required for the computation of the RVE response to macroscopic boundary conditions, which was in a similar range for both the 3D and 2.5D approach. Therefore, the 3D model raises the computational costs significantly if the network generation hast to be repeated multiple times, e.g. in a parametric study, or as part of on iterative process in an inverse FE analysis.

In conclusion, for networks with high porosity the 2.5D approach represents an efficient and reliable alternative to full 3D modelling as regards the in-plane mechanics of ESNs. The 3D model, on the other hand, covers the whole range of porosities. Furthermore, it opens the door for the investigation of relevant aspects of ESNs such as the types of fibre junctions, contacts and shapes, the dependence of material properties on fibre diameter, and the presence of different fibre types in co-spinning.

Appendix A. Convergence studies

In order to determine the necessary size of a RVE, networks with increasing dimensions were generated (Sec. 2.2). The fibre geometry was defined as sine-shaped ($\alpha_F = 7\mu m$, $\Lambda_F = 150\mu m$) with circular cross section ($d_F = 1\mu m$) and the fibre material was defined linear elastic ($E_F = 1500MPa$, $\nu_F = 0.4$). The body force $\boldsymbol{g}$ was kept constant leading to networks with average porosity ϕ=0.967. Uniaxial loading was performed for every network until five percent of global elongation in loading direction ($\lambda = 1.05$) was reached. The elastic energy density as a kinetic variable and the

lateral contraction as a kinematic metric were evaluated from the results to investigate their dependence on network size. In a first step, the thickness t_N was increased for a constant width $b_N = 300\mu m$ of the square in-plane region $b_N \times b_N$ (Fig. A.1ab). In a second step, the width b_N was increased keeping the thickness constant ($t_N \approx 30\mu m$, see Fig. A.1cd). To reduce the influence of the random microstructure, simulations were conducted for $N = 3$ realisations per size. The results are summarised in figure A.1 where dimensions were normalised by fibre diameter ($\bar{t}_N = t_N/d_F$, $\bar{b}_N = b_N/d_F$). Both measures, the lateral contraction and the energy density, show convergence for increasing network size.

To assure that the explicit integration scheme as well as both inertia and damping forces, have negligible influence on the results three more simulations for a representative network (Sec. 3.5, σ_{d_F}=0.2) were conducted. For each simulation either time step (Δt), macroscopic strain rate ($\dot{\varepsilon}$) or damping constant (α_R), was reduced to half of its original value and the macroscopic response of the network was compared to the original simulation (Fig. A.1e). No significant difference could be observed, confirming the choices used for the computations in the present paper.

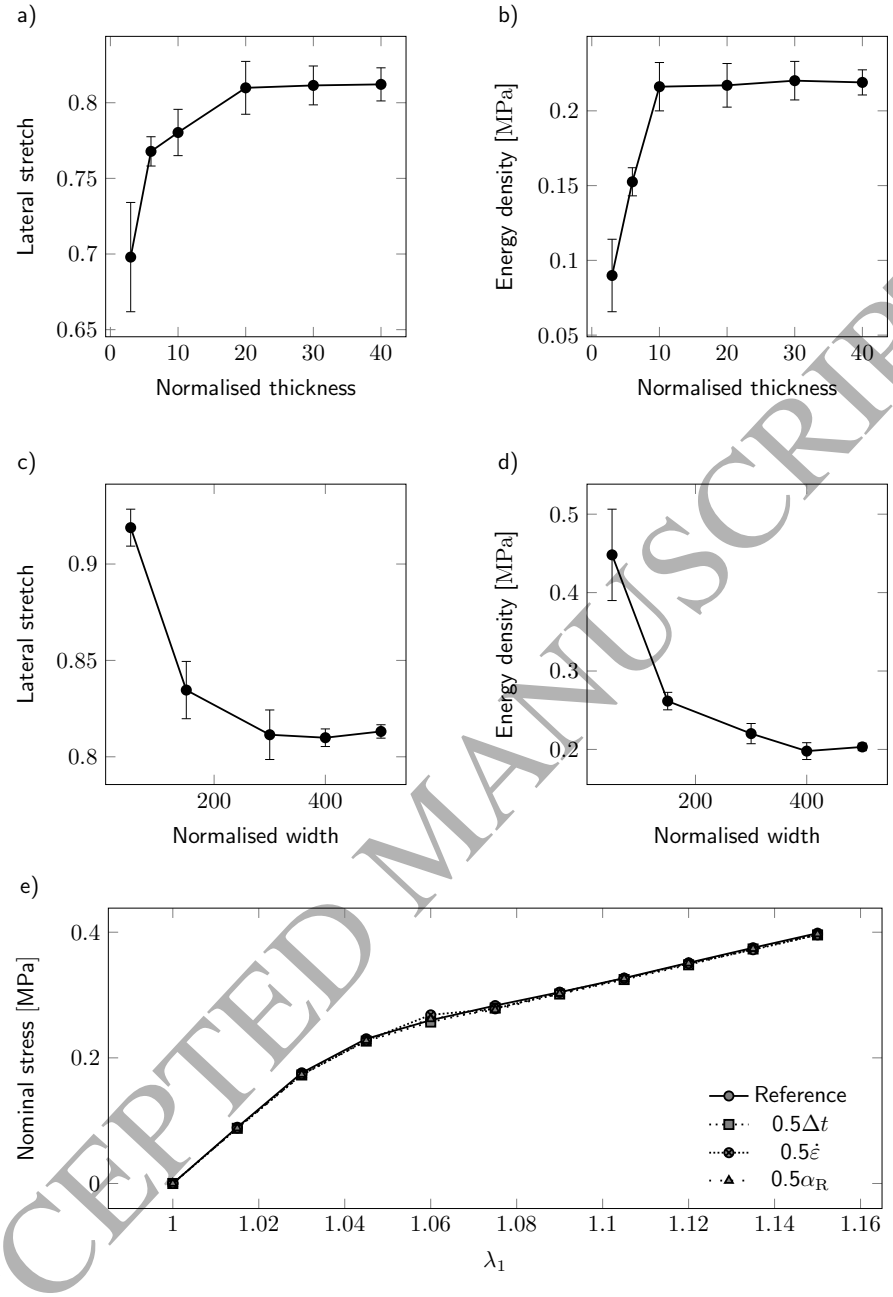

Figure A.1: **a-d)** Convergence study with regard to RVE size. Lateral contraction **(a,c)** and elastic energy density **(b,d)** for uniaxial tension at 5% applied stretch ($\lambda_{\mathrm{f}} = 1.05$) for different RVE thicknesses **(a,b)** and edge lengths **(c,d)**. RVE dimensions were normalized by fibre diameter d_{F}. Results are shown as mean and standard deviation (error bars) for $N = 3$ realizations. **e)** Verification of parameters used for explicit intergration by reducing their values.

Acknowledgements

This work was partly supported by the Swiss National Science Foundation under grant no. 155918.

References

References

[1] D. Li, Y. Xia, Electrospinning of nanofibers: Reinventing the wheel?, Advanced Materials 16 (2004) 1151–1170.

[2] L. J. Villarreal-Gómez, J. M. Cornejo-Bravo, R. Vera-Graziano, D. Grande, Electrospinning as a powerful technique for biomedical applications: a critically selected survey, Journal of Biomaterials Science, Polymer Edition 27 (2016) 157–176.

[3] J. Fang, H. Niu, T. Lin, X. Wang, Applications of electrospun nanofibers, Chinese Science Bulletin 53 (2008) 2265–2286.

[4] T. J. Sill, H. A. von Recum, Electrospinning: Applications in drug delivery and tissue engineering, Biomaterials 29 (2008) 1989 – 2006.

[5] S. Mohammadzadehmoghadam, Y. Dong, I. J. Davies, Modelling electrospun nanofibers: An overview from theoretical, empirical, and numerical approaches, International Journal of Polymeric Materials and Polymeric Biomaterials (2016).

[6] J. H. Wendorff, S. Agarwal, A. Greiner, Electrospinning: materials, processing, and applications, John Wiley & Sons, 2012.

[7] J. Melcher, G. Taylor, Electrohydrodynamics: a review of the role of interfacial shear stresses, Annual review of fluid mechanics 1 (1969) 111–146.

[8] B. G. Xu, H. F. Guo, Numerical study of taylor cone dynamics in electrospinning of nanofibers, in: Innovative Materials: Engineering and Applications II, volume 730 of *Key Engineering Materials*, Trans Tech Publications, 2017, pp. 510–515.

[9] E. Mazza, A. E. Ehret, Mechanical biocompatibility of highly deformable biomedical materials, Journal of the Mechanical Behavior of Biomedical Materials 48 (2015) 100 – 124.

[10] N. Nerurkar, D. Elliott, R. Mauck, Mechanics of oriented electrospun nanofibrous scaffolds for annulus fibrosus tissue engineering, Journal of Orthopaedic Research 25 (2007) 1018–1028.

[11] N. Nerurkar, R. Mauck, D. Elliott, ISSLS prize winner: integrating theoretical and experimental methods for functional tissue engineering of the annulus fibrosus., Spine 33 (2008) 2691–2701.

[12] N. L. Nerurkar, R. L. Mauck, D. M. Elliott, Modeling interlamellar interactions in angle-ply biologic laminates for annulus fibrosus tissue engineering, Biomechanics and Modeling in Mechanobiology 10 (2011) 973–984.

[13] B. Baker, N. Nerurkar, J. Burdick, D. Elliott, R. Mauck, Fabrication and modeling of dynamic multipolymer nanofibrous scaffolds, Journal of Biomechanical Engineering 131 (2009).

[14] C.-L. Pai, M. Boyce, G. Rutledge, On the importance of fiber curvature to the elastic moduli of electrospun nonwoven fiber meshes, Polymer 52 (2011) 6126–6133.

[15] M. N. Silberstein, C.-L. Pai, G. C. Rutledge, M. C. Boyce, Elastic-plastic behavior of non-woven fibrous mats, Journal of the Mechanics and Physics of Solids 60 (2012) 295 – 318.

[16] G. Limbert, R. Omar, H. Krynauw, D. Bezuidenhout, . Franz, The anisotropic mechanical behaviour of electro-spun biodegradable polymer scaffolds: Experimental characterisation and constitutive formulation, Journal of the Mechanical Behavior of Biomedical Materials 53 (2016) 21–39.

[17] R. D. Vita, D. J. Leo, K. D. Woo, C. Nah, A constitutive law for poly(butylene terephthalate) nanofibers mats, Journal of Applied Polymer Science 102 (2006) 5280–5283.

[18] T. Courtney, M. S. Sacks, J. Stankus, J. Guan, W. R. Wagner, Design and analysis of tissue engineering scaffolds that mimic soft tissue mechanical anisotropy, Biomaterials 27 (2006) 3631–3638.

[19] J.-J. Hu, Constitutive modeling of an electrospun tubular scaffold used for vascular tissue engineering, Biomechanics and Modeling in Mechanobiology 14 (2015) 897–913.

[20] M. Rizvi, P. Kumar, D. Katti, A. Pal, Mathematical model of mechanical behavior of micro/nanofibrous materials designed for extracellular matrix substitutes, Acta Biomaterialia 8 (2012) 4111 – 4122.

[21] M. S. Rizvi, A. Pal, Statistical model for the mechanical behavior of the tissue engineering non-woven fibrous matrices under large deformation, Journal of the Mechanical Behavior of Biomedical Materials 37 (2014) 235 – 250.

[22] A. Shahsavari, R. Picu, Size effect on mechanical behavior of random fiber networks, International Journal of Solids and Structures 50 (2013) 3332 – 3338.

[23] S. Borodulina, H. Motamedian, A. Kulachenko, Effect of fiber and bond strength variations on the tensile stiffness and strength of fiber networks, International Journal of Solids and Structures (2016).

[24] S. Goutianos, R. Mao, T. Peijs, Effect of inter-fibre bonding on the fracture of fibrous networks with strong interactions, International Journal of Solids and Structures (2017).

[25] M. Ostoja-Starzewski, Lattice models in micromechanics, Applied Mechanics Reviews 55 (2002) 35–60.

[26] A. Kulachenko, T. Uesaka, Direct simulations of fiber network deformation and failure, Mechanics of Materials 51 (2012) 1 – 14.

[27] A. Ridruejo, C. González, J. LLorca, Damage micromechanisms and notch sensitivity of glass-fiber non-woven felts: An experimental and numerical study, Journal of the Mechanics and Physics of Solids 58 (2010) 1628 – 1645.

[28] T. Stylianopoulos, V. H. Barocas, Volume-averaging theory for the study of the mechanics of collagen networks, Computer Methods in Applied Mechanics and Engineering 196 (2007) 2981 – 2990.

[29] A. Mauri, R. Hopf, A. E. Ehret, C. R. Picu, E. Mazza, A discrete network model to represent the deformation behavior of human amnion, Journal of the Mechanical Behavior of Biomedical Materials 58 (2016) 45 – 56.

[30] A. E. Ehret, K. Bircher, A. Stracuzzi, V. Marina, M. Zündel, E. Mazza, Inverse poroelasticity as a fundamental mechanism in biomechanics and mechanobiology, Nature Communications 8 (2017) 1002.

[31] B. Agoram, V. Barocas, Coupled macroscopic and microscopic scale modeling of fibrillar tissues and tissue equivalents, Journal of Biomechanical Engineering 123 (2001) 362–369.

[32] T. Stylianopoulos, C. A. Bashur, A. S. Goldstein, S. A. Guelcher, V. H. Barocas, Computational predictions of the tensile properties of electrospun fibre meshes: Effect of fibre diameter and fibre orientation, Journal of the mechanical behavior of biomedical materials 1 (2008) 326–335.

[33] G. Argento, M. Simonet, C. Oomens, F. Baaijens, Multi-scale mechanical characterization of scaffolds for heart valve tissue engineering, Journal of biomechanics 45 (2012) 2893–2898.

[34] X. Wei, Z. Xia, S.-C. Wong, A. Baji, Modelling of mechanical properties of electrospun nanofibre network, International Journal of Experimental and Computational Biomechanics 1 (2009) 45–57.

[35] A. Agic, B. Mijovic, Mechanical properties of electrospun carbon nanotube composites, The Journal of The Textile Institute 97 (2006) 419–427.

[36] B. Mijovic, A. Agic, Bio-inspired electrospun fibre structures-numerical model, Journal of Fiber Bioengineering and Informatics 6 (2013) 23–32.

[37] A. D'Amore, N. Amoroso, R. Gottardi, C. Hobson, C. Carruthers, S. Watkins, W. R. Wagner, M. S. Sacks, From single fiber to macro-level mechanics: A structural finite-element model for elastomeric fibrous biomaterials, Journal of the Mechanical Behavior of Biomedical Materials 39 (2014) 146 – 161.

[38] Y. Liu, Y. Dzenis, Explicit 3D finite-element model of continuous nanofibre networks, Micro & Nano Letters 11 (2016) 727–730.

[39] A. D'Amore, J. A. Stella, W. R. Wagner, M. S. Sacks, Characterization of the complete fiber network topology of planar fibrous tissues and scaffolds, Biomaterials 31 (2010) 5345–5354.

[40] J. B. Carleton, G. J. Rodin, M. S. Sacks, Layered elastomeric fibrous scaffolds: An in-silico study of the achievable range of mechanical behaviors, ACS Biomaterials Science & Engineering 3 (2017) 2907–2921.

[41] M. Zündel, E. Mazza, A. E. Ehret, A 2.5D approach to the mechanics of electrospun fibre mats, Soft Matter 13 (2017) 6407–6421.

[42] B. R. Neugirg, S. R. Koebley, H. C. Schniepp, A. Fery, AFM-based mechanical characterization of single nanofibres, Nanoscale 8 (2016) 8414–8426.

[43] R. Inai, M. Kotaki, S. Ramakrishna, Structure and properties of electrospun plla single nanofibres, Nanotechnology 16 (2005) 208.

[44] V. Cnudde, M. N. Boone, High-resolution X-ray computed tomography in geosciences: A review of the current technology and applications, Earth-Science Reviews 123 (2013) 1–17.

[45] U. Stachewicz, P. K. Szewczyk, A. Kruk, A. H. Barber, A. Czyrska-Filemonowicz, Pore shape and size dependence on cell growth into electrospun fiber scaffolds for tissue engineering: 2d and 3d analyses using sem and fib-sem tomography, Materials Science and Engineering: C (2017).

[46] K. Niskanen, M. J. Alava, Planar random networks with flexible fibers, Physical review letters 73 (1994) 3475.

[47] H. Altendorf, D. Jeulin, Random-walk-based stochastic modeling of three-dimensional fiber systems, Physical Review E 83 (2011) 041804.

[48] J. Carleton, A. D'Amore, K. Feaver, G. Rodin, M. Sacks, Geometric characterization and simulation of planar layered elastomeric fibrous biomaterials, Acta Biomaterialia 12 (2015) 93–101.

[49] D. Durville, Numerical simulation of entangled materials mechanical properties, Journal of Materials Science 40 (2005) 5941–5948.

[50] N. Saitô, K. Takahashi, Y. Yunoki, The statistical mechanical theory of stiff chains, Journal of the Physical Society of Japan 22 (1967) 219–226.

[51] O. Kratky, G. Porod, Diffuse small-angle scattering of X-rays in colloid systems, Journal of colloid science 4 (1949) 35–70.

[52] C. Rivetti, M. Guthold, C. Bustamante, Scanning force microscopy of DNA deposited onto mica: Equilibration versus kinetic trapping studied by statistical polymer chain analysis, Journal of molecular biology 264 (1996) 919–932.

[53] G. Lamour, J. Kirkegaard, H. Li, T. Knowles, J. Gsponer, Easyworm: An open-source software tool to determine the mechanical properties of worm-like chains, Source Code for Biology and Medicine 9 (2014).

[54] J. Bednar, P. Furrer, V. Katritch, A. Stasiak, J. Dubochet, A. Stasiak, Determination of DNA persistence length by cryo-electron microscopy. Separation of the static and dynamic contributions to the apparent persistence length of DNA, Journal of Molecular Biology 254 (1995) 579 – 594.

[55] F. Gittes, B. Mickey, J. Nettleton, J. Howard, Flexural rigidity of microtubules and actin filaments measured from thermal fluctuations in shape., The Journal of cell biology 120 (1993) 923–934.

[56] L. Sivakumar, G. Agarwal, The influence of discoidin domain receptor 2 on the persistence length of collagen type I fibers, Biomaterials 31 (2010) 4802 – 4808.

[57] C. Walck, Hand-book on statistical distributions for experimentalists, Technical Report, 1996.

[58] Abaqus, Documentation, Dassault Systèmes, Providence, RI, USA, 2016.

[59] X. Zhang, R. Nakagawa, K. Chan, M. Kotaki, Mechanical property enhancement of polylactide nanofibers through optimization of molecular weight, electrospinning conditions, and stereocomplexation, Macromolecules 45 (2012) 5494–5500.

[60] F. Chen, X. Peng, T. Li, S. Chen, X.-F. Wu, D. H. Reneker, H. Hou, Mechanical characterization of single high-strength electrospun polyimide nanofibres, Journal of Physics D: Applied Physics 41 (2008) 025308.

[61] J. S. Soares, W. Zhang, M. S. Sacks, A mathematical model for the determination of forming tissue moduli in needled-nonwoven scaffolds, Acta Biomaterialia (2017) –.

[62] J. Lannutti, D. Reneker, T. Ma, D. Tomasko, D. Farson, Electrospinning for tissue engineering scaffolds, Materials Science and Engineering: C 27 (2007) 504 – 509.

[63] T. Toniatto, B. Rodrigues, T. Marsi, R. Ricci, F. Marciano, T. Webster, A. Lobo, Nanostructured poly (lactic acid) electrospun fiber with high loadings of TiO_2 nanoparticles: Insights into bactericidal activity and cell viability, Materials Science and Engineering: C 71 (2017) 381–385.

[64] X. Zhu, W. Cui, X. Li, Y. Jin, Electrospun fibrous mats with high porosity as potential scaffolds for skin tissue engineering, Biomacromolecules 9 (2008) 1795–1801.

[65] S. Ramakrishna, An Introduction to Electrospinning and Nanofibers, 2005.

[66] C. E. Ayres, B. S. Jha, H. Meredith, J. R. Bowman, G. L. Bowlin, S. C. Henderson, D. G. Simpson, Measuring fiber alignment in electrospun scaffolds: a user's guide to the 2D fast Fourier transform approach, Journal of Biomaterials Science, Polymer Edition 19 (2008) 603–621.

[67] L. Zhang, W. Yu, Orientation image analysis of electrospun submicro-fibers based on hough transform and regionprops function, Textile Research Journal (2016).

[68] J. Deitzel, J. Kleinmeyer, D. Harris, N. B. Tan, The effect of processing variables on the morphology of electrospun nanofibers and textiles,

Polymer 42 (2001) 261 – 272.